


**Nonmonotonic interfacial friction with normal force in two-dimensional crystals**Hao Li,<sup>\*</sup> Wenhao Shi,<sup>\*</sup> Yufeng Guo<sup>✉,†</sup> and Wanlin Guo<sup>‡</sup>*State Key Laboratory of Mechanics and Control of Mechanical Structures and MOE Key Laboratory for Intelligent Nano Materials and Devices, College of Aerospace Engineering, Nanjing University of Aeronautics and Astronautics, Nanjing 210016, China* (Received 26 October 2019; revised 22 February 2020; accepted 13 August 2020; published 25 August 2020)

Classic Amontons' law states that friction force increases monotonically with the increase of normal force. Here a nonmonotonic variation of interfacial friction with normal force is revealed in two-dimensional van der Waals bilayers by extensive first-principles calculations. The results show that the interlayer sliding energy barriers and shear strengths of MoS<sub>2</sub>, hexagonal boron nitride, and graphene bilayers turn to decrease with the relative movement of top and bottom monolayers from the lowest to the highest energy stacking state under normal pressures beyond 1.8, 14.7, and 7.6 GPa, respectively. Meanwhile, the interlayer binding energy differences between the highest and the lowest energy stacking state are nonmonotonic as the normal pressure increases. This anomalous frictional behavior in two-dimensional crystals is effectively interpreted by the opposite contributions of interlayer van der Waals and Coulomb interactions.

DOI: [10.1103/PhysRevB.102.085427](https://doi.org/10.1103/PhysRevB.102.085427)

Classic Amontons' law states that friction force between two sliding solid surfaces is always proportional to the applied normal force or the friction coefficient is constant, as the real contact area is proportional to the normal force [1–3]. Scaling down to the nanometer regime, Amontons' law is valid in most cases [4–7], but occasionally broken in some specific situations [8–12]. For example, negative friction coefficient was found at the interface between graphene sheets and the tip of atomic force microscope when the tip is detached away from the graphene sheets [8,9], or between graphene and hexagonal boron nitride (h-BN) due to load-induced suppression of out-of-plane distortion [10]. However, under compressive normal force or further increase of normal force, the friction will increase again with normal force even in these specific systems.

An important fact is that natural layered crystals such as graphite, h-BN, and molybdenum disulfide (MoS<sub>2</sub>) are conventional solid lubricants for heavy-duty machinery or extreme pressure environments [13,14]. These layered crystals are widely recognized to hold together by weak interfacial van der Waals (vdW) interactions. Lubricant additives based on nanosheets of layered vdW crystals could significantly reduce friction and wear under high contact pressure [15,16]. Extensive studies have shown that when the thicknesses of vdW crystals decrease to their atomic limits, the friction properties may become quite different from their bulk states [17–22]. Two-dimensional (2D) vdW crystals such as graphene and MoS<sub>2</sub> could possess ultralow friction depending on stacking commensurability [23,24], substrate adhesion [25,26], out-of-plane stiffness [17], and interface structure [27–30]. Theoretical simulations are important tools to study friction

properties at nanoscale. However, most first-principles works on interlayer friction of 2D vdW crystal are conducted by constant interlayer distance mode rather than constant normal-force mode. There is still a lack of extensive investigation on how the interfacial friction of 2D vdW crystal changes with normal load.

In this work, we find through first-principles calculations employing constant normal-force mode that the interfacial friction in commensurate MoS<sub>2</sub>, h-BN, and graphene bilayers is nonmonotonic under high normal pressure, and the interlayer sliding energy barrier and resistance turn to decrease with the increase of normal pressure. The underlying mechanism of this unconventional frictional behavior is comprehensively elucidated by analyzing the variations of interlayer vdW and Coulomb energy barriers with normal pressure and the contributions of electron kinetic and electrostatic energies to interlayer Coulomb interaction. These results could deepen our understanding of lubricating performance of 2D vdW crystal in heavy loading environment.

Figure 1 shows the models of 2H MoS<sub>2</sub>, h-BN, and graphene bilayers with initial AB stacking in the rhombus unit cells, where each MoS<sub>2</sub>, h-BN, and graphene monolayer consists of 1 Mo and 2 S atoms, 1 B and 1 N atoms, and 2 C atoms, respectively. A vacuum region larger than 25 Å is in the direction perpendicular to the plane. All computations were performed within the framework of density-functional theory (DFT) as implemented in the FHI-aims code with “tight” computational settings [31] in which the Perdew-Burke-Ernzerhof (PBE) [32] or hybrid Heyd-Scuseria-Ernzerhof (HSE06) [33] exchange-correlation functional is employed. The influence of vdW interactions is considered by using a many-body dispersion (MBD) vdW model [34,35]. A *k*-point grid of 15 × 15 × 1 was used throughout the work. First the whole systems were relaxed by PBE+MBD until the force on each atom is less than 0.001 eV/Å. The optimized lattice constants of MoS<sub>2</sub>, h-BN, and graphene unit cells are 3.166, 2.507, and

<sup>\*</sup>These authors contributed equally to this work.<sup>†</sup>yfguo@nuaa.edu.cn<sup>‡</sup>wlguo@nuaa.edu.cn

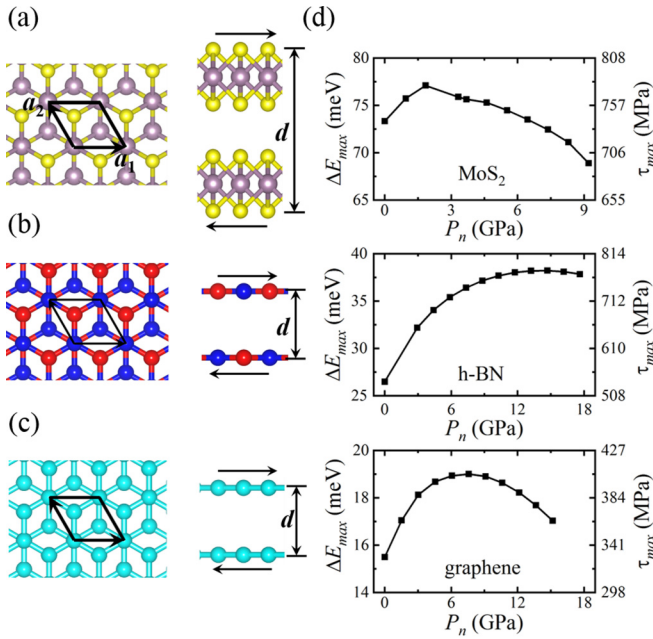


FIG. 1. Atomic structures of (a) MoS<sub>2</sub>, (b) h-BN, and (c) graphene bilayers with AB stacking. The purple, yellow, blue, red, and cyan balls are Mo, S, N, B, and C atoms, respectively. Here  $d$  is the interlayer distance between top and bottom monolayers. (d) Variations of the maximum sliding energy barrier  $\Delta E_{\max}$  and shear strength  $\tau_{\max}$  against the applied normal pressure  $P_n$ . The arrows denote the interlayer sliding of the bilayers.

2.467 Å, respectively. To simulate interlayer sliding, the top monolayer is transversely moved with respect to the bottom monolayer and shifts relatively to different stacking positions on the  $a_1 - a_2$  plane where the nearest translational positions are separated by 0.396, 0.313, and 0.308 Å for MoS<sub>2</sub>, h-BN, and graphene, respectively. The interlayer distances  $d$  of the vdW bilayers are modified by changing the  $z$ -direction coordinates of the atoms in the top layers. For graphene and h-BN bilayers, 1 C and 1 B atoms in the top layers and 1 C and 1 B atoms in the bottom layers are fully fixed at each shifted position. For MoS<sub>2</sub> bilayer, only the S atoms at the top and bottom surfaces are fully fixed. Then those systems were relaxed again by PBE+MBD and the normal forces at different interlayer distances and stacking positions were calculated by summing the  $z$ -direction forces of all atoms in one monolayer. In this way, interlayer sliding simulation of the vdW bilayer under constant normal-force mode is realized. As shown in Supplemental Material, Figs. S1–S3(a) [36], the deviations between the desired normal force and normal forces at different shifted positions are less than 1%. To maintain a constant normal force, the interlayer distance  $d$  between two monolayers varies with the stacking position; see Figs. S1–S3(b) [36]. After relaxation, the total energies at different stacking positions were calculated using HSE+MBD, and the corresponding potential energy surface for interlayer sliding under a given normal force  $F_n$  was constructed by  $\Delta E = E - E_{\min}$ , where the  $E$  is the total energy of the system and  $E_{\min}$  is the lowest total energy; see Figs. S1–S3(c) [36]. The normal pressure  $P_n$  is calculated by  $P_n = F_n/A$ , where  $A$  is the area of unit cell.

For all the graphene, MoS<sub>2</sub>, and h-BN bilayers, the highest and lowest total energies under a given normal force are found to be at AA and AB stacking states, respectively. We calculated the maximum sliding energy barrier  $\Delta E_{\max}$  by  $\Delta E_{\max} = E_{AA} - E_{AB}$ , and the maximum interlayer resistance force  $F_R^{\max}$  and shear strength  $\tau_{\max}$  [20] by  $F_R^{\max} = \Delta E_{\max}/\Delta r$  and  $\tau_{\max} = F_R^{\max}/A$ , where  $\Delta r$  is the displacement along the pathway from the lowest to the highest energy stacking state. The interlayer friction force of a vdW bilayer is proportional to  $\Delta E_{\max}$  [37]. As shown in Fig. 1(d),  $\Delta E_{\max}$  and  $\tau_{\max}$  of the three bilayer systems increase first with increasing normal pressure, obeying the traditional friction law, but turn to decrease after the normal pressure becomes high enough, leading to a nonmonotonic variation of friction with normal pressure. Correspondingly, the friction coefficient becomes negative under high normal pressure. The critical normal pressures are 1.8 GPa (MoS<sub>2</sub>), 14.7 GPa (h-BN), and 7.6 GPa (graphene), respectively. Compared with graphene and h-BN, MoS<sub>2</sub> bilayers show the largest decrease in  $\Delta E_{\max}$  and  $\tau_{\max}$ , and turn to decrease at the lowest critical normal pressure, showing the strongest nonmonotonic friction behavior.

Interlayer friction of a vdW bilayer is closely related to interlayer adhesion or binding interaction. So, we calculated the interlayer binding energy  $E_{\text{binding}}$  by  $E_{\text{binding}} = E_{\text{bilayer}} - E_{\text{monolayer}}^t - E_{\text{monolayer}}^b$ , and the interlayer binding energy difference  $\Delta E_b$  between AA and AB stacking by  $\Delta E_b = E_{\text{binding}}^{AA} - E_{\text{binding}}^{AB}$ , where  $E_{\text{bilayer}}$  is the total energy of the bilayer, and  $E_{\text{monolayer}}^t$  and  $E_{\text{monolayer}}^b$  are the total energies of top and bottom monolayers, respectively. In Figs. 2(a)–2(c), it can be seen that  $\Delta E_b$  is approximately the same as  $\Delta E_{\max}$  in all three vdW bilayer systems, although the value for MoS<sub>2</sub> bilayer is larger than that for other two vdW bilayers. When the vdW bilayer slides under constant interlayer distance mode, the interlayer distance deviation  $\Delta d$  ( $\Delta d = d_{AA} - d_{AB}$ ) between AA and AB stacking is zero. Under constant normal-force mode, as shown in the insets of Fig. 2,  $\Delta d$  of MoS<sub>2</sub> bilayer decreases with increasing normal pressure while  $\Delta d$  of graphene and h-BN systems first decrease and then increase but the variations in  $\Delta d$  of graphene and h-BN systems are slight.

The vdW and Coulomb interactions are usually the main contributions to interlayer adhesion or binding interaction. We calculated the interlayer vdW energy  $E_{\text{vdW}}$  at different stacking positions by  $E_{\text{vdW}} = E_{\text{vdW}}^{\text{bilayer}} - E_{\text{vdW}}^t - E_{\text{vdW}}^b$ , where  $E_{\text{vdW}}^{\text{bilayer}}$  is the total vdW energy of the bilayer,  $E_{\text{vdW}}^t$  and  $E_{\text{vdW}}^b$  are the vdW energies of top and bottom monolayers, respectively. The interlayer Coulomb energy  $E_{\text{Coul}}$  can be obtained by  $E_{\text{Coul}} = E_{\text{binding}} - E_{\text{vdW}}$  and the values of  $E_{\text{Coul}}$  are all positive. Detailed interlayer vdW, binding, and Coulomb energy surfaces during sliding can be seen in Figs. S4–S6 [36]. The differences in interlayer vdW energy  $\Delta \text{vdW}$  and Coulomb energy  $\Delta E_c$  between AA stacking and AB stacking are calculated by  $\Delta \text{vdW} = E_{\text{vdW}}^{AA} - E_{\text{vdW}}^{AB}$  and  $\Delta E_c = E_{\text{Coul}}^{AA} - E_{\text{Coul}}^{AB}$ , respectively. From the definition of  $\Delta E_b$ ,  $\Delta E_c$ , and  $\Delta \text{vdW}$ , we have  $\Delta E_b = \Delta \text{vdW} + \Delta E_c$ . As shown in Fig. 3(a), the contributions of interlayer vdW and Coulomb interactions to interlayer friction are opposite in MoS<sub>2</sub> bilayer in the whole calculating range. In graphene and h-BN, the contributions of interlayer vdW and Coulomb interactions also become opposite under high normal pressure, although

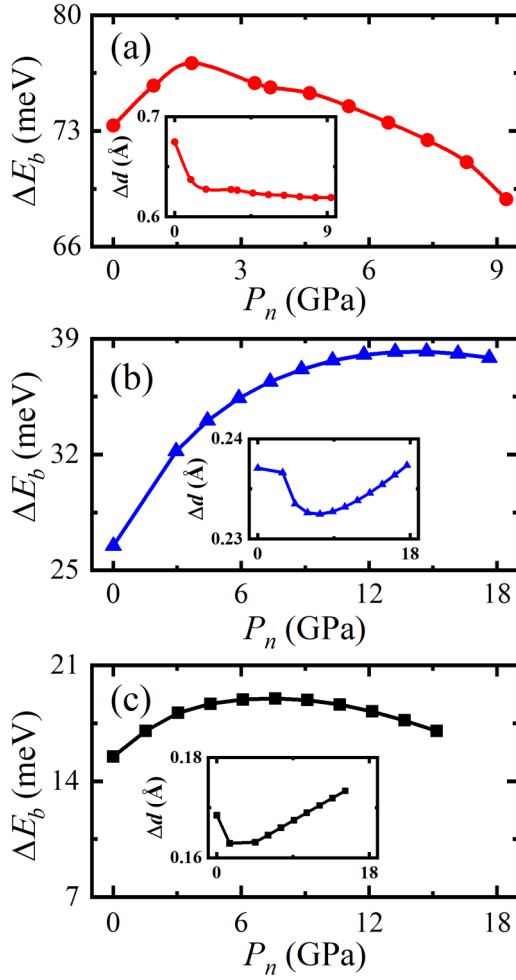


FIG. 2. The interlayer binding energy differences  $\Delta E_b$  of (a) MoS<sub>2</sub> (red), (b) h-BN (blue), and (c) graphene (black) bilayers under different normal pressures. The insets show the corresponding interlayer distance deviations  $\Delta d$ .

they take the same increasing trend at lower normal pressure. The interlayer vdW energy differences  $\Delta \text{vdW}$  of the three vdW bilayers monotonically increase with the increase of normal pressure. As  $\Delta \text{vdW}$  of graphene bilayer is lower than that of MoS<sub>2</sub> and h-BN bilayers, the contribution of interlayer vdW interaction to interlayer friction is larger in polar vdW bilayers, coinciding with the previous study [38]. In contrast,  $\Delta E_c$  of graphene and h-BN turn to decrease under high normal pressure, which accordingly reduces the interlayer sliding energy barrier. For MoS<sub>2</sub> bilayer,  $\Delta E_c$  is always negative and monotonically decreases with the normal pressure increases, hence the interlayer Coulomb repulsion is weaker at AA stacking and counteracts the effect of interlayer vdW interaction on interlayer friction. The nonmonotonic interlayer friction behavior and friction reduction in the vdW bilayers thus can be attributed to the significant decrease in interlayer Coulomb energy barrier or the counteracting effect from interlayer Coulomb interaction.

The total energy consists of kinetic, electrostatic, exchange-correlation, and vdW energy. To better understand the role of interlayer Coulomb interaction, we separately calculated the energy differences in exchange-correlation

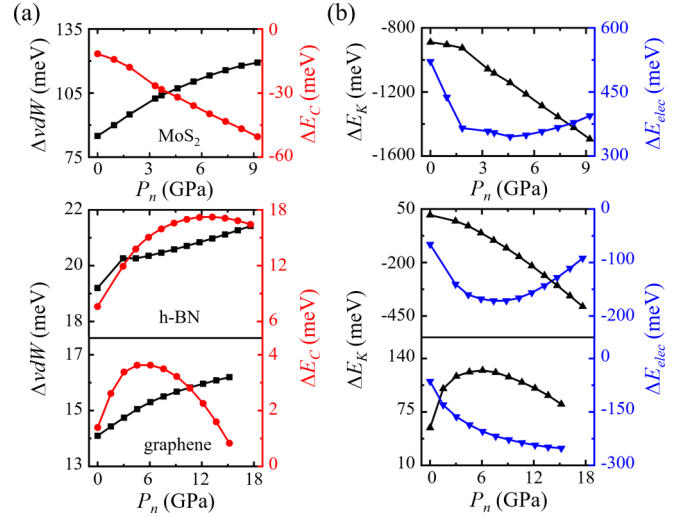


FIG. 3. Variations of the differences in energy components between AA and AB stacking against the normal pressure for MoS<sub>2</sub>, h-BN, and graphene bilayers. (a) The differences in vdW energy  $\Delta \text{vdW}$  (square) and Coulomb energy  $\Delta E_c$  (circle). (b) The differences in kinetic energy  $\Delta E_K$  (up triangle) and electrostatic energy  $\Delta E_{\text{elec}}$  (down triangle).

energy  $\Delta E_{XC}$ , kinetic energy  $\Delta E_K$ , and electrostatic energy  $\Delta E_{\text{elec}}$  between AA and AB stacking by  $\Delta E_{XC} = (E_{XC}^{\text{bilayer}} - E_{XC}^t - E_{XC}^b)_{AA} - (E_{XC}^{\text{bilayer}} - E_{XC}^t - E_{XC}^b)_{AB}$ ,  $\Delta E_K = (E_K^{\text{bilayer}} - E_K^t - E_K^b)_{AA} - (E_K^{\text{bilayer}} - E_K^t - E_K^b)_{AB}$ , and  $\Delta E_{\text{elec}} = (E_{\text{elec}}^{\text{bilayer}} - E_{\text{elec}}^t - E_{\text{elec}}^b)_{AA} - (E_{\text{elec}}^{\text{bilayer}} - E_{\text{elec}}^t - E_{\text{elec}}^b)_{AB}$ , where  $t$  and  $b$  denote the top and bottom monolayers, respectively. We have  $\Delta E_c = \Delta E_{XC} + \Delta E_K + \Delta E_{\text{elec}}$ . The exchange-correlation energy barriers  $\Delta E_{XC}$  of the three vdW bilayers monotonically increase with increasing normal pressure; see Fig. S7 [36]. For graphene bilayer, the kinetic energy barrier  $\Delta E_K$  first increases and then decreases with normal pressure, but the electrostatic energy barrier  $\Delta E_{\text{elec}}$  monotonically decreases, as shown by Fig. 3(b). The negative values of  $\Delta E_{\text{elec}}$  and  $\Delta E_K$  in Fig. 3(b) represent lower electrostatic and kinetic energies at AA stacking. In the cases of MoS<sub>2</sub> and h-BN,  $\Delta E_K$  monotonically decrease with the increase of normal pressure, while  $\Delta E_{\text{elec}}$  first decrease and then increase. For all three bilayers, the monotonic increase in exchange-correlation energy difference  $\Delta E_{XC}$  suggests that Pauli repulsion is stronger at AA stacking and the effect of Pauli repulsion increases with the increase of normal pressure. The contributions of kinetic and electrostatic energies to interlayer Coulomb interaction are similar in MoS<sub>2</sub> and h-BN bilayers but different in graphene bilayer. In graphene, the decrease in kinetic and electrostatic energy barriers leads to a smaller interlayer Coulomb energy barrier. A lower kinetic energy barrier means that the electrons move closer to the nuclei when the bilayer slides to AA stacking. For MoS<sub>2</sub> and h-BN bilayers, the kinetic energies at AA stacking are lower than that at AB stacking. The significant reduction in kinetic energy at AA stacking induces the counteracting effect of interlayer Coulomb interaction in MoS<sub>2</sub> and weakens the interlayer Coulomb energy barrier of h-BN under high normal pressure. Furthermore, the charge-density

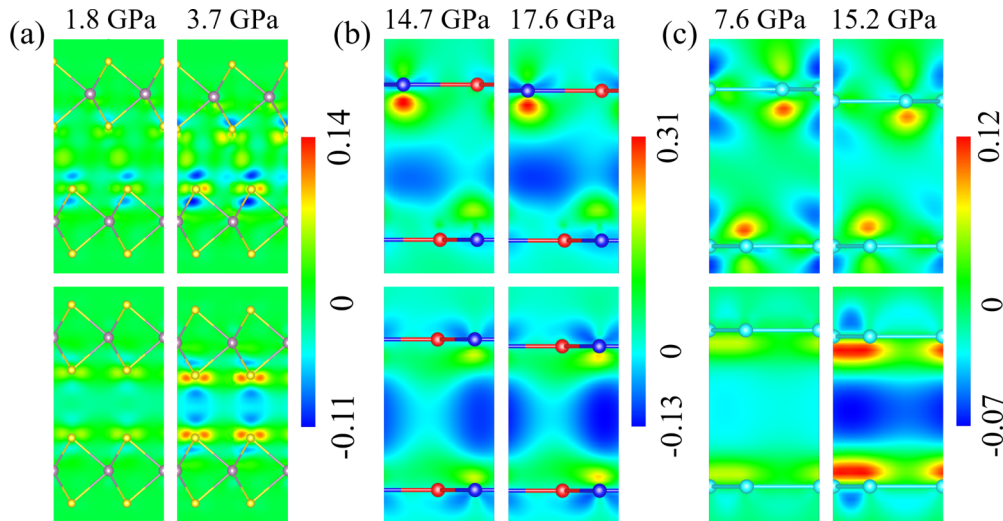


FIG. 4. 2D projections of charge-density differences  $\Delta\rho$  (in units of  $e/\text{\AA}^3$ ) of (a) MoS<sub>2</sub>, (b) h-BN, and (c) graphene bilayers at *AB* stacking (top) and *AA* stacking (bottom) under different normal pressures. The 1.8 GPa in (a), 14.7 GPa in (b), and 7.6 GPa in (c) are the critical normal pressures at which  $\Delta E_{\text{max}}$  are the largest. The ball denotation is the same as Fig. 1.

differences  $\Delta\rho$  at *AB* and *AA* stacking were calculated by  $\Delta\rho = \rho_{\text{bilayer}} - \rho_{\text{monolayer}}^{\text{top}} - \rho_{\text{monolayer}}^{\text{bottom}}$ . As shown in Fig. 4, charge transfer and exchange occur at the interfaces of the vdW bilayers. Compared with *AB* stacking, interlayer charge depletions of the three bilayers are stronger at *AA* stacking and charge distribution becomes more homogeneous on the interface atoms. Charge accumulations on the S, C, and N atoms at *AA* stacking increase with increasing normal pressure. The charge redistribution at *AA* stacking shown in Fig. 4 is consistent with the decrease in kinetic energy barrier. For h-BN, more electrons move to the N atoms due to stronger electronegativity. The homogeneity of charge distribution on the B and N atoms of h-BN bilayer at *AA* stacking is weaker than that on the S atoms of MoS<sub>2</sub> and C atoms of graphene at *AA* stacking, which provides a reasonable explanation for the slight decrease of  $\Delta E_{\text{max}}$  in h-BN bilayer under high normal pressure.

By using the same procedure and method with HSE+MBD, we have studied interlayer frictional behaviors of initial *AA'* stacked MoS<sub>2</sub> and h-BN bilayers. It can be seen from the variations of  $\Delta E_{\text{max}}$  in Figs. S8 and S9 [36] that the interfacial friction in MoS<sub>2</sub> and h-BN bilayers with *AA'* stacking is still nonmonotonic with the increase of normal pressure. The same as the initial *AB* stacking state, the decrease in interlayer Coulomb energy barrier and counteracting effect give rise to the nonmonotonic variation of interlayer friction; see Figs. S8(c) and S9(c) [36]. Moreover, the interlayer frictional behaviors of the vdW bilayers have been investigated by another DFT method with the PBE exchange-correlation functional [32,39,40] and optB86b for vdW interaction [41,42].  $\Delta E_{\text{max}}$  and  $\tau_{\text{max}}$  in graphene and MoS<sub>2</sub> bilayers obtained by PBE+optB86b qualitatively coincide with that by HSE+MBD, but in h-BN bilayer the PBE+optB86b result fluctuates with normal pressure; see Fig. S13 [36]. This inconsistency in h-BN bilayer between HSE+MBD and PBE+optB86b is possibly due to the low accuracy of the optB86b model in describing the long-range vdW interaction for nonhomogeneous electron

densities in 2D h-BN [38,43,44]. In spite of the difference in the two vdW models, the interlayer friction in h-BN bilayer still exhibits nonmonotonic trend. Similarly, the anomalous interfacial friction is also attributed to the opposite contributions of interlayer vdW and Coulomb interactions; see Fig. S14 [36].

For comparison, interfacial friction of graphene and MoS<sub>2</sub> bilayers under constant interlayer distance mode has been studied by PBE+optB86b. The maximum sliding energy barriers monotonically increase with the decrease of interlayer distance, and the normal forces vary with the stacking position; see Figs. S15–S17 [36]. To better explain such discrepancy between constant normal force and constant interlayer distance mode, we established two *AB* and *AA* stacked graphene sheets in which each sheet consists of 8 C layers; see Fig. S18 [36]. At the fixed distance of 48.5 Å between the top and bottom layers, the ratio of normal force at *AA* stacking to that at *AB* stacking is 1.27 and decreases to 1.11 when the distance is reduced to 47.5 Å; see Table S1 [36]. Due to weak interlayer vdW adhesion, the thickness of 8-layer graphene sheet decreases after normal loading, so that the actual change in the interface distance between two 8-layer graphene sheets is relatively small. The thickness compressibility leads to a smaller deviation in the normal forces at different stacking positions. For a vdW monolayer, the normal load is hard to change the thickness because of single atom layer or strong Mo–S bond. Previous DFT simulations under constant interlayer distance mode [20] show that interlayer friction of bilayer graphene still satisfies Amontons-like law when normal pressure is up to 160 GPa. However, under constant normal-force mode as Amontons' law required, friction turns to decrease with increasing normal pressure beyond 1.8, 14.7, and 7.6 GPa for MoS<sub>2</sub>, h-BN, and graphene, respectively. The *sp*<sup>2</sup> graphene will turn to *sp*<sup>3</sup> diamondlike phase at normal pressure beyond about 18 GPa [45], and the diamondlike phase will collapse beyond normal pressure  $\sim 120$  GPa. As a consequence, the interfacial frictional behavior of vdW bilayer under constant normal-force mode displays unexpected

trend compared with that under commonly used constant interlayer distance mode.

In summary, we show by comprehensive DFT calculations that under constant normal-force mode, the interfacial friction and shear resistance in 2D vdW bilayers are nonmonotonic with the increase of normal pressure. Bilayer MoS<sub>2</sub>, h-BN, and graphene exhibit interlayer friction reduction and negative friction coefficients under viable high normal pressure. The opposite contributions of interlayer vdW and Coulomb interactions result in such anomalous frictional behavior. These results unveil a special interfacial friction law when the thick-

ness of vdW crystals decreases to the atomic limit, and deepen our understanding of efficient lubrication in 2D vdW crystals under heavy working conditions.

This work is supported by the NSFC (Grants No. 11622218, No. 11972186, No. 11890674, No. 51921003, and No. 51535005), the NSF of Jiangsu Province (Grant No. BK20160037), the Fundamental Research Funds for the Central Universities (Grant No. NE2019001) of China, and a project funded by the Priority Academic Program Development of Jiangsu Higher Education Institutions.

- 
- [1] F. P. Bowden and D. Tabor, *The Friction and Lubrication of Solids* (Oxford University Press, Oxford, 2001).
- [2] D. Dowson, *History of Tribology* (Addison-Wesley Longman, London, 1979).
- [3] B. N. J. Persson, *Sliding Friction: Physical Principles and Applications* (Springer Science & Business Media, Berlin, 2013).
- [4] J. Gao, W. D. Luedtke, D. Gourdon, M. Ruths, J. N. Israelachvili, and U. Landman, Frictional forces and Amontons' law: From the molecular to the macroscopic scale, *J. Phys. Chem. B* **108**, 3410 (2004).
- [5] M. R. Vazirisereshk, H. Ye, Z. Ye, A. Otero-de-la-Roza, M. Zhao, Z. Gao, A. T. C. Johnson, E. R. Johnson, R. W. Carpick, and A. Martini, Origin of nanoscale friction contrast between supported graphene, MoS<sub>2</sub>, and a graphene/MoS<sub>2</sub> heterostructure, *Nano Lett.* **19**, 5496 (2019).
- [6] Y. Liu, A. Song, Z. Xu, R. Zong, J. Zhang, W. Yang, R. Wang, Y. Hu, J. Luo, and T. Ma, Interlayer friction and superlubricity in single-crystalline contact enabled by two-dimensional flake-wrapped atomic force microscope tips, *ACS Nano* **12**, 7638 (2018).
- [7] S. Liu, H. Wang, Q. Xu, T. Ma, G. Yu, C. Zhang, D. Geng, Z. Yu, S. Zhang, W. Wang, Y. Hu, H. Wang, and J. Luo, Robust microscale superlubricity under high contact pressure enabled by graphene-coated microsphere, *Nat. Commun.* **8**, 14029 (2017).
- [8] Z. Deng, A. Smolyanitsky, Q. Li, X. Feng, and R. Cannara, Adhesion-dependent negative friction coefficient on chemically modified graphite at the nanoscale, *Nat. Mater.* **11**, 1032 (2012).
- [9] A. Smolyanitsky and J. Killgore, Anomalous friction in suspended graphene, *Phys. Rev. B* **86**, 125432 (2012).
- [10] D. Mandelli, W. Ouyang, O. Hod, and M. Urbakh, Negative Friction Coefficients in Superlubric Graphite–Hexagonal Boron Nitride Heterojunctions, *Phys. Rev. Lett.* **122**, 076102 (2019).
- [11] L. Gao, Y. Ma, Y. Liu, A. Song, T. Ma, Y. Hu, Y. Su, and L. Qiao, Anomalous frictional behaviors of Ir and Au tips sliding on graphene/Ni(111) substrate: Density functional theory calculations, *J. Phys. Chem. C* **121**, 21397 (2017).
- [12] M. C. Righi and M. Ferrario, Pressure Induced Friction Collapse of Rare Gas Boundary Layers Sliding over Metal Surfaces, *Phys. Rev. Lett.* **99**, 176101 (2007).
- [13] A. Savan, E. Pflüger, P. Voumard, A. Schröer, and M. Simmonds, Modern solid lubrication: Recent developments and applications of MoS<sub>2</sub>, *Lubr. Sci.* **12**, 185 (2000).
- [14] J. Xu, M. Zhu, Z. Zhou, P. Kapsa, and L. Vincent, An investigation on fretting wear life of bonded MoS<sub>2</sub> solid lubricant coatings in complex conditions, *Wear* **255**, 253 (2003).
- [15] D. Mishra, F. J. Sonia, D. Srivastava, G. N. Ganesha, U. Singha, and A. Mukhopadhyay, Wear damage and effects of graphene-based lubricants/coatings during linear reciprocating sliding wear at high contact pressure, *Wear* **400**, 144 (2018).
- [16] A. Ahmadi, J. Tang, V. G. Pol, F. Sadeghi, and K. K. Mistry, Binder mediated enhanced surface adhesion of cured dry solid lubricant on bearing steel for significant friction and wear reduction under high contact pressure, *Carbon* **146**, 588 (2019).
- [17] C. Lee, Q. Li, W. Kalb, X. Liu, H. Berger, R. W. Carpick, and J. Home, Frictional characteristics of atomically thin sheets, *Science* **328**, 76 (2010).
- [18] J. S. Choi, J. Kim, I. Byun, D. H. Lee, M. J. Lee, B. H. Park, C. Lee, D. Yoon, H. Cheong, and K. H. Lee *et al.*, Friction anisotropy-driven domain imaging on exfoliated monolayer graphene, *Science* **333**, 607 (2011).
- [19] S. Li, Q. Li, R. W. Carpick, P. Gumbsch, X. Liu, X. Ding, J. Sun, and J. Li, The evolving quality of frictional contact with graphene, *Nature (London)* **539**, 541 (2016).
- [20] J. Sun, Y. Zhang, Z. Lu, Q. Li, Q. Xue, S. Du, J. Pu, and L. Wang, Superlubricity enabled by pressure-induced friction collapse, *J. Phys. Chem. Lett.* **9**, 2554 (2018).
- [21] J. Sun, Y. Lu, Y. Feng, Z. Lu, G. Zhang, Y. Yuan, and L. Qian, Friction-load relationship in the adhesive regime revealing potential incapability of AFM investigations, *Tribol. Lett.* **68**, 18 (2020).
- [22] W. Ouyang, I. Azuri, D. Mandelli, A. Tkatchenko, L. Kronik, M. Urbakh, and O. Hod, Mechanical and tribological properties of layered materials under high pressure: Assessing the importance of many-body dispersion effects, *J. Chem. Theory Comput.* **16**, 666 (2020).
- [23] M. Dienwiebel, G. S. Verhoeven, N. Pradeep, J. W. M. Frenken, J. A. Heimberg, and H. W. Zandbergen, Superlubricity of Graphite, *Phys. Rev. Lett.* **92**, 126101 (2004).
- [24] Y. F. Guo, W. L. Guo, and C. F. Chen, Modifying atomic-scale friction between two graphene sheets: A molecular-force-field study, *Phys. Rev. B* **76**, 155429 (2007).
- [25] Q. Li, C. Lee, R. Carpick, and J. Hone, Substrate effect on thickness-dependent friction on graphene, *Phys. Status Solidi B* **247**, 2909 (2010).

- [26] D. Cho, L. Wang, J. Kim, G. Lee, E. S. Kim, S. Lee, S. Y. Lee, J. Hone, and C. Lee, Effect of surface morphology on friction of graphene on various substrates, *Nanoscale* **5**, 3063 (2013).
- [27] Z. Ye, A. Balkanci, A. Martini, and M. Z. Baykara, Effect of roughness on the layer-dependent friction of few-layer graphene, *Phys. Rev. B* **96**, 115401 (2017).
- [28] A. Smolyanitsky, J. P. Killgore, and V. K. Tewary, Effect of elastic deformation on frictional properties of few-layer graphene, *Phys. Rev. B* **85**, 035412 (2012).
- [29] X. Zheng, L. Gao, Q. Yao, Q. Li, M. Zhang, X. Xie, S. Qiao, G. T. Ma, Z. Di, J. Luo, and X. Wang, Robust ultra-low-friction state of graphene via moiré superlattice confinement, *Nat. Commun.* **7**, 13204 (2016).
- [30] H. Li, J. Wang, S. Gao, Q. Chen, L. Peng, K. Liu, and X. Wei, Superlubricity between MoS monolayers, *Adv. Mater.* **29**, 1701474 (2017).
- [31] V. Blum, R. Gehrke, F. Hanke, P. Havu, V. Havu, X. Ren, K. Reuter, and M. Scheffler, Ab initio molecular simulations with numeric atom-centered orbitals, *Comput. Phys. Commun.* **180**, 2175 (2009).
- [32] J. P. Perdew, K. Burke, and M. Ernzerhof, Generalized Gradient Approximation Made Simple, *Phys. Rev. Lett.* **77**, 3865 (1996).
- [33] J. Heyd, G. E. Scuseria, and M. Ernzerhof, Hybrid functionals based on a screened coulomb potential, *J. Chem. Phys.* **118**, 8207 (2003).
- [34] A. Tkatchenko, A. Ambrosetti, and R. A. DiStasio Jr., Interatomic methods for the dispersion energy derived from the adiabatic connection fluctuation-dissipation theorem, *J. Chem. Phys.* **138**, 074106 (2013).
- [35] A. Tkatchenko, R. A. DiStasio Jr., R. Car, and M. Scheffler, Accurate and Efficient Method for Many-Body Van Der Waals Interactions, *Phys. Rev. Lett.* **108**, 236402 (2012).
- [36] See Supplemental Material at <http://link.aps.org/supplemental/10.1103/PhysRevB.102.085427> for the calculation details and the results by PBE+optB86b.
- [37] A. Socoliuc, R. Bennewitz, E. Gnecco, and E. Meyer, Transition from Stick-Slip to Continuous Sliding in Atomic Friction: Entering a New Regime of Ultralow Friction, *Phys. Rev. Lett.* **92**, 134301 (2004).
- [38] W. Gao and A. Tkatchenko, Sliding Mechanisms in Multilayered Hexagonal Boron Nitride and Graphene: The Effects of Directionality, Thickness, and Sliding Constraints, *Phys. Rev. Lett.* **114**, 096101 (2015).
- [39] G. Kresse and J. Furthmüller, Efficient iterative schemes for ab initio total-energy calculations using a plane-wave basis set, *Phys. Rev. B* **54**, 11169 (1996).
- [40] P. E. Blöchl, Projector augmented-wave method, *Phys. Rev. B* **50**, 17953 (1994).
- [41] J. Klimeš, D. R. Bowler, and A. Michaelides, Chemical accuracy for the van der Waals density functional, *J. Phys.: Condens. Matter* **22**, 022201 (2009).
- [42] J. Klimeš, D. R. Bowler, and A. Michaelides, Van der Waals density functionals applied to solids, *Phys. Rev. B* **83**, 195131 (2011).
- [43] T. Bučko, S. Lebègue, J. G. Ángyán, and J. Hafner, Extending the applicability of the Tkatchenko-Scheffler dispersion correction via iterative Hirshfeld partitioning, *J. Chem. Phys.* **141**, 034114 (2014).
- [44] T. Bučko, S. Lebègue, T. Gould, and J. G. Ángyán, Many-body dispersion corrections for periodic systems: An efficient reciprocal space implementation, *J. Phys.: Condens. Matter* **28**, 045201 (2016).
- [45] W. L. Guo, C. Z. Zhu, T. X. Yu, C. H. Woo, B. Zhang, and Y. T. Dai, Formation of  $sp^3$  Bonding in Nanoindented Carbon Nanotubes and Graphite, *Phys. Rev. Lett.* **93**, 245502 (2004).